

Sensing, Detection and Localization for Low Altitude UAV: A RF-Based Framework via Multiple BSs Collaboration

Tianhao Liang, *Member, IEEE*, Mu Jia, Tingting Zhang, *Member, IEEE*, Junting Chen, *Member, IEEE*, Longyu Zhou, *Member, IEEE*, Tony Q. S. Quek, *Fellow, IEEE*, and Pooi-Yuen Kam, *Life Fellow, IEEE*

Abstract—The rapid growth of the low-altitude economy has resulted in a significant increase in the number of low, slow, and small (LSS) unmanned aerial vehicles (UAVs), raising critical challenges for secure airspace management and reliable trajectory planning. To address this, this paper proposes a cooperative radio-frequency (RF) detection and localization framework that leverages existing cellular base stations. The proposed approach features a robust scheme for LSS target identification, integrating a cell averaging-constant false alarm rate (CA-CFAR) detector with a micro-Doppler signature (MDS) based recognition method. Multi-station measurements are fused through a grid-based probabilistic algorithm combined with clustering techniques, effectively mitigating ghost targets and improving localization accuracy in multi-UAV scenarios. Furthermore, the Cramer-Rao lower bound (CRLB) is derived as a performance benchmark and reinforcement learning (RL)-based optimization is employed to balance localization accuracy against station resource usage. Simulations demonstrate that increasing from one to multiple BSs reduces the positioning error to near the CRLB, while practical experiments further verify the framework’s effectiveness. Furthermore, our RL-based optimization can find solutions that maintain high accuracy while minimizing resource usage, highlighting its potential as a scalable solution for ensuring airspace safety in the emerging low-altitude economy.

Index Terms—Low altitude economy, UAV detection, cooperative localization, data fusion, Cramer-Rao bound.

I. INTRODUCTION

A. Background and Motivation

Driven by the advancements in Unmanned aerial vehicle (UAV) technologies and supportive governmental policies, the low-altitude economy is experiencing rapid expansion from ground into the airspace. This growing promotes a wide range of emerging aerial applications, including logistics, emergency rescue, situation awareness, and environmental monitoring

Tianhao Liang and Tingting Zhang are with Guangdong Provincial Key Laboratory of Aerospace Communication and Networking Technology, School of Information Science and Technology, Harbin Institute of Technology (Shenzhen), Shenzhen, P.R. China. Tingting Zhang is also with Pengcheng Laboratory (PCL), Shenzhen, P.R. China. Mu Jia, Junting Chen, Pooi-Yuen Kam are with the School of Science and Engineering, Shenzhen Future Network of Intelligence Institute (FNII-Shenzhen), and Guangdong Provincial Key Laboratory of Future Networks of Intelligence, The Chinese University of Hong Kong, Shenzhen, Guangdong 518172, P.R. China. Longyu Zhou is with Information System Technology and Design, Singapore University of Technology and Design and also with ChinaTelecom Singapore Innovation Research Institute. Tony Q. S. Quek is with Information System Technology and Design Pillar, Singapore University of Technology and Design, Singapore. (e-mail: liangth@hit.edu.cn; mujial@link.cuhk.edu.cn; zhangtt@hit.edu.cn; juntingc@cuhk.edu.cn; zhoullyfuture@outlook.com; tonyquek@sutd.edu.sg; pykam@cuhk.edu.cn).

[1]–[7]. Concurrently, this trend is leading to an unprecedented increase in the number of UAVs, which introduces complex challenges to airspace management and flight safety [8]–[10].

On the one hand, diverse low-altitude services involve heterogeneous UAV types and mission requirements [11]. In the absence of interconnectivity among these applications, UAVs from different services can act as non-cooperative aerial obstacles. Their trajectories need to be accurately sensed, detected and localized to enable collision avoidance and improve flight efficiency [12], [13]. On the other hand, the extensive use of UAVs may raise the risk of unauthorized and non-cooperative drones operations, posing potential threats to public safety, such as terrorist attack, smuggling, and the disruptions to the normal operations of critical infrastructure like airports, military strongholds and large hydroelectric plants [14]–[16]. Consequently, there is a pressing need for robust and reliable UAV sensing, detection and localization technologies, which are not only vital to ensure secure and reliable low-altitude operations, but also essential for supporting the sustainable development of the low-altitude economy [17]–[21].

To achieve accurate detection accuracy, vision-based method have been investigated as mainstream UAV detection schemes [22]. However, their performance degrades in occluded and low-light environments. In contrast, radio frequency (RF)-based methods can work all-time and all-weather, making them priority alternatives for robust UAV detection [23], [24]. Generally, achieving high sensing, detection and localization accuracy in practice requires the deployment of numerous dedicated devices, which significantly increases infrastructure costs and prohibit their adoption in a short time [25]. Prompted by the advancement of millimeter wave and integrated sensing and communication (ISAC) technologies for the upcoming sixth-generation (6G) networks, sensing functions can be performed directly by base stations (BSs) without requiring additional equipments [26]–[31]. Inspired by investigations of the ISAC applications for aerial scenarios, UAV sensing, detection and localization can be implemented using the current cellular networks, offering a cost-effective and scalable solution by unifying spectral resources and hardware platforms [32]–[34].

Despite the growing attention to UAV sensing, detection and localization via BSs, practical operations still faces several key limitations [35], [36], presented below.

- UAVs in low-altitude applications are typically small targets, with a radar cross section (RCS) under 2m^2 , and their speeds are usually not exceeding 200km/h. These

characteristics classify them as low-slow-small (LLS) aerial targets, which are inherently difficult to distinguish from background clutter in urban environments, as they exhibit a low signal-to-clutter-plus-noise ratio and weak Doppler signatures [37]–[39].

- In highly dynamic low-altitude environments, many existing solutions exhibit excessive computational complexity, leading them difficult to satisfy real-time sensing, detection and localization requirements [40], [41].
- Most importantly, the complex propagation environments in urban and low-altitude settings create significant multipath reflections. These reflections can generate false observations, named “ghost” targets, which severely degrade the accuracy and reliability of target detection [42]–[45].

These limitations highlight the urgent exploration for more advanced sensing, detection and localization frameworks of LLS targets within existing networks to meet the safety and reliability requirements of the emerging low-altitude economy.

Motivated by these challenges, this paper focuses on reliable UAV detection and localization by leveraging existing BSs, thereby reducing the need for costly dedicated sensing infrastructure. Utilizing the antenna array at the BS, the hybrid time of arrival (ToA) and angle of arrival (AoA) method can be employed to obtain ranging and angle information from the UAV using pilot or ISAC signals [46], [47]. To enhance the detection and localization performance of BSs, the inherent Doppler modulation caused by the rotation of UAV’s rotor, named micro-Doppler signature (MDS), can be exploited to obtain the more concentrated energy of LLS UAV targets [48] [49]. Furthermore, the cooperative scheme among multiple BSs and the efficient methods for processing multiple UAV targets recognition are necessary to be designed to eliminate ghost interference and enhance localization accuracy [50], which is the focus of this investigation.

B. Related Works

UAV detection and localization by multiple stations can be briefly divided into three key phases [51]. The first is parameter estimation process, where localization-related information (e.g., distance and angle) is extracted from the received RF signals. The second phase involves clutter suppression and feature extraction operations, which are critical for mitigating interference from the environment and distinguishing UAV targets from noise and ghost reflections. The last stage is the cooperative data fusion process, where information from multiple stations is combined to refine the final position of the UAV and improve overall accuracy [52]. In the following, we overview the related works corresponding to each of these three stages.

For UAV detection and localization, the estimation process of UAV parameters is determined by the localization method. Common methods include ToA, AoA, received signal strength (RSS), and their combinations [53]. Generally, RSS is usually applied in indoor localization systems due to its feasibility and simplicity. However, it exhibits low accuracy in environments with significant fading or unknown pathloss coefficient [54], [55]. Conversely, ToA and AoA methods can provide relative

higher accuracy distance measurements, especially for large bandwidth signals. Due to the synchronization issues, the ToA measurements can be further categorized into time difference of arrival (TDOA) and round trip measuring methods [56]. Different from traditional distributed multiple input multiple output (MIMO) radar system [57], the asynchronous problem has been effectively addressed in currently BS architectures. To fully utilize the capabilities of these BSs, the hybrid TOA and AOA is often adopted to locate the detected targets, which has been proven to yield excellent localization performance [58]–[60].

Clutters caused by the scatterers are the useless components in the received signals and must be suppressed. The key of clutter suppression is analyzing the property of clutter according to the relationship between scatterers and receiver systems [61]. For static reflectors and slow-moving clutter, benefited from the increased stability of digital processor, the moving target indicator (MTI) filters are effective at isolating targets with significant velocity [62]. However, for the dynamic LLS UAV targets with weak Doppler signatures, it is difficult to obtain high detection performance through the traditional detectors like constant false alarm rate (CFAR) [63] and adaptive normalized matched filter (AMF) [64]. To overcome this issue, method based on the MDS have been extensively investigated. Typically, the echo of rotor UAV mainly includes the translational component generated by the motion of UAV’s body and the micro-Doppler component generated by the rotation of rotor, whose echo is a typical sine frequency modulation (SFM) signal [65]. Therefore, by properly exploiting the micro-Doppler effects, target recognition can be significantly improved [66]. Generally, time-frequency analysis methods, such as short-time Fourier transform (STFT), radon-Wigner transform (RWT), etc., are used to generate the time-frequency spectrogram representing the MDS [67], [68]. Features are then extracted from these spectrograms using transition methods like singular value decomposition (SVD) [69], empirical mode decomposition (EMD) [70]. Subsequently, the LLS UAV can be detected using classification methods, such as support vector machines (SVM), and convolutional neural networks (CNN) [71], [72].

The multipath propagation generated by random reflectors or unexpected obstacles is another critical issue during detection process, especially in the complicated environment [73]. Compared to traditional long range detection, sensing inside the low-altitude scenarios suffers much more from the multipath effects, which leads to severe detection performance degradation and ghost targets generation [74]. Without proper priori knowledge of the environment, these ghosts could be mapped back to their corresponding true target location, which cause severe interference to the environmental sensing and mapping. Typically, two different ghost targets can be generated both from measurement procedure and data fusion phases, respectively. There may exist multipath ghosts produced by the indirect path propagations for an individual transmitter, with different bounce process from the reflector [75]. Additionally, multiple targets inside the beam intersection areas from multiple transmitter can also generate ghost detections [76]. These ghost targets will lead to unexpected false alarms, which

has attracted wide interests [77], [78]. Consequently, various techniques for ghost suppression have been investigated. In [75], based on the phase property of multipath ghost, the phase coherent factor (PCF) was weighted to the radar image, to mitigate the ghost power. The authors in [79] found out the physical relationship among target, first-order ghost and second-order ghost. The Hough transform was applied to find out real target in range-Doppler domain. Machine learning based methods have also been adopted to recognize the ghost from measured observations. After training with the pre collected data from vehicle radar, the ghost can be distinguished successfully [80]. Building a cooperative sensor network is one of the most effective method to suppress ghost. The authors in [78] analyzed the aspect properties of ghost target, and introduced a sensor network with multiple monostatic radars to mitigate the ghost and realize indoor tracking. In [81], a distributed MIMO radar network was deployed, to sequentially separate the ghosts out.

The design of cooperative schemes, encompassing both the fusion method and node selection strategy, is also crucial for the detection and localization performance in a multiple-station network, especial for those resource limited scenarios. The geometric configuration of the participating station directly affects the detection and localization performance due to the difference in received signal intensity [82]. A straightforward method is to reduce the resource cost on BS nodes, to increase the positioning accuracy while conserving power and reducing interference between sensing communication [83]. Many investigations leverage the Cramer-Rao Lower Bound (CRLB), which provides a theoretical minimum for localization error, as a metric for optimizing the joint allocation of network resources like energy and spectrum [84] [85]. Nevertheless, the CRLB is not always achievable in low SNR conditions. To address this limitation, reinforcement learning (RL) based methods have been proposed. These approaches can optimize a non-closed-form localization metric, such as the mean square error (MSE) output by a specific algorithm, making them more practical for real-world scenarios with varying SNR [86], [87].

C. Contribution

To address aforementioned challenges while fully leveraging current infrastructures, we propose a multi-layered, RF-based cooperative framework for UAV sensing, detection, and localization. Our approach begins with robust single-station sensing for LLS targets by combination methods of CA-CFAR detector and MDS based algorithm. Subsequently, measurements from multiple stations are intelligently fused using a grid-based probabilistic algorithm, which incorporates clustering to handle multi-UAV scenarios and effectively mitigate ghost targets. To improve the network efficiency, we introduce a RL-based optimization strategy that adaptively balances the localization accuracy and the number of involved stations. The main contributions of this paper are summarized as follows.

- We first establish the framework for low altitude UAV sensing and detection, which is founded on a hybrid TOA and AOA localization method. The ghost types caused by indirect propagations are also analyzed comprehensively.

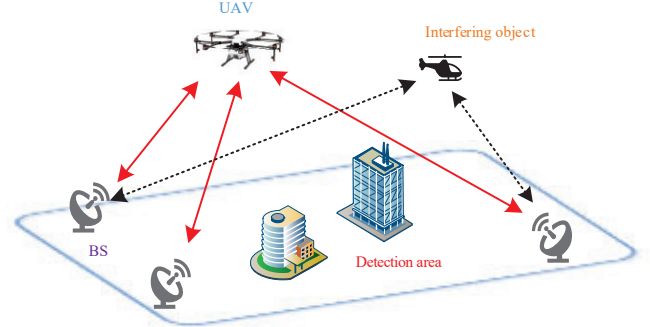


Fig. 1. System model for multi-BS collaborative UAV detection in a complex low-altitude environment.

- A CA-CFAR algorithm is then proposed to suppress clutters and obtain the ranging and angle information from received signals. The MDS-based methodology using EMD is employed to recognize the LLS UAV and further improve detection performance.
- Subsequently, a clustering based method is provided in multi-UAV scenarios, where a probabilistic grid-based data fusion method is proposed to mitigate the ghost targets and enhance the localization accuracy.
- The CRLB is derived analytically to illustrate the theoretical performance limits of this cooperative localization network. Two joint localization accuracy and node selection optimization problems are formulated and solved by RL-based algorithm to optimize the network efficiency. Numerical simulations and practical experiments are conducted to validate the superiority and feasibility of proposed framework.

The rest of this paper is organized as follows. Section II introduces the system model, detailing the measuring signal and ghost generation types. Section III presents algorithms of signal parameters estimation, MDS extraction and data fusion for UAV sensing, detection and localization, respectively. In section IV, the CRLB is derived, and two optimization problems are formulated and solved. Subsequently, simulation results and illustrated experiments are carried out in section V. Finally, Section VI draws the conclusion and key findings of this paper.

II. SYSTEM MODEL

A. Scenario

As depicted in Fig. 1, we consider a low-altitude surveillance scenario in the urban. There are N_{BS} BSs deployed to monitor a specific area of interest. Within this area, there may be one or more non-cooperative UAVs to be detected and localized. There are also some other unintentional moving objects (e.g., helicopters, birds) and a number of randomly located interactive objects, such as high buildings and other cooperative aerial devices. These interactive objects act as reflectors and are the primary source of multipath propagation, which can generate ghost echoes. Each BS attempts to detect and localize UAVs based on received echoes. The primary focus of this work is to recognize and locate the UAV

by intelligently fusing the observations from all individual stations. The investigation is carried out based on the following key assumptions:

- The received echoes at BSs may be generated by the UAV, unintentional targets, and randomly located interactive objects. The presence and location of interactive objects may vary over time due to the dynamic nature of the environment.
- The interactive objects are treated as uncorrelated scatterers. For simplicity in modeling multipath, we primarily consider single-interaction bounces.
- During the detection interval (a single coherent processing interval), the UAVs are assumed to be quasi-static, meaning their velocity is constant and their position does not change significantly.

B. Signal Model

Generally, the received signal $r(t)$ at the BS, superposed by the signals from UAVs and ghosts, can be expressed as

$$r(t) = \sum_{i=0}^{N_t} A_i S(t - \tau_i(t)) + \sum_{j=N_t+1}^{N_t+N_g+1} A_j S(t - \tau_j(t)) + w(t), \quad (1)$$

where $S(t)$ represents the transmitted signal, and $w(t)$ is additive white Gaussian noise (AWGN). The first summation accounts for the echoes from the N_t real UAVs, while the second part represents the echoes from the N_g multipath ghosts in the environment. The term A_i is the amplitude of the received signal from the i -th scatterer, which is determined by the radar range equation and expressed as

$$A_i = \sqrt{\frac{P_{tx} G_{tx} G_{rx} \lambda^2 \sigma_i}{(4\pi)^3 R_i^4}}. \quad (2)$$

Here, P_{tx} is the transmit power, G_{tx} and G_{rx} are the transmit and receive antenna gains, respectively, λ is the signal wavelength, and R is the distance to the scatterer. The term σ_i indicates the RCS of the i th scatterer.

The term $\tau_i(t)$ is time delay of the signal reflected from UAV i , which is a function of its range and velocity. Assuming a UAV is at an initial distance R_i from the BS and moving with a radial velocity v_i , the two-way time delay can be expressed as

$$\tau_i(t) = 2(R_i + v_i t)/c, \quad (3)$$

where c is the speed of light in free space.

To enable angle estimation, we assume each BS is equipped with a uniform linear array (ULA) consisting of K antenna elements. The signal received at the k -th element of the array, $r_k(t)$, can be modeled based on the signal at the first element and a phase shift corresponding to the angle of arrival

$$r_k(t) = r_0(t) \exp(j \frac{2\pi}{\lambda} d_{an}(k-1) \sin \theta), \quad (4)$$

where $r_0(t)$ is the received signal at the first antenna element, and d_{an} is the distance between adjacent antenna elements, and θ is the AoA of the signal from the UAV.

C. Ghost Target Generation

In complex low-altitude environments, signals will propagate along multiple paths before returning to the receiver, leading to the generation of “ghost” targets, which are false detections.

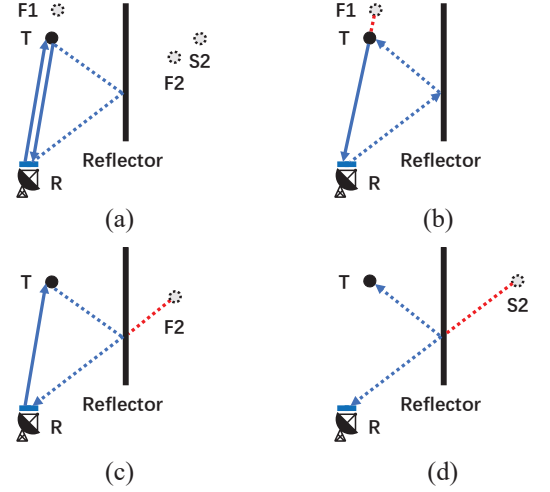


Fig. 2. Geometry types of multipath ghost generation.

To illustrate the properties of multipath ghosts, we consider a detection scenario with one BS, one UAV, and one reflector, as shown in Fig. 2. The signal transmitted by the BS is assumed to be received by both the UAV and the reflector within its field of view (FoV). Ghosts are detected due to these indirect signal reflections. Based on the propagation path, these received signals can be categorized into the following types.

- 1) **Direct Path:** As shown in Fig. 2(a), the direct or line-of-sight path follows the propagation BS→UAV→BS. This corresponds to the real detection of the UAV.
- 2) **Type-1 First-Order Ghost:** This ghost involves a reflection off the reflector before the signal illuminates the UAV. As shown in Fig. 2(b), it experiences the propagation path BS→Reflector→UAV→BS.
- 3) **Type-2 First-Order Ghost:** This ghost, shown in Fig. 2(c), occurs when the signal reflects off the reflector after scattering from the UAV. The propagation path is BS→UAV→Reflector→BS.
- 4) **Second-Order Ghost:** Fig. 2(d) shows a second-order ghost, where both the transmitted and received signals bounce off the reflector. The path is BS→Reflector→UAV→Reflector→BS¹.

The detection probability of both the real UAV and the multipath ghosts is highly related to their signal-to-noise ratio

¹If multiple reflectors exist, a signal may experience more than two indirect reflections. Generally, the energy of these higher-order ghosts is relatively small, making them less likely to be detected.

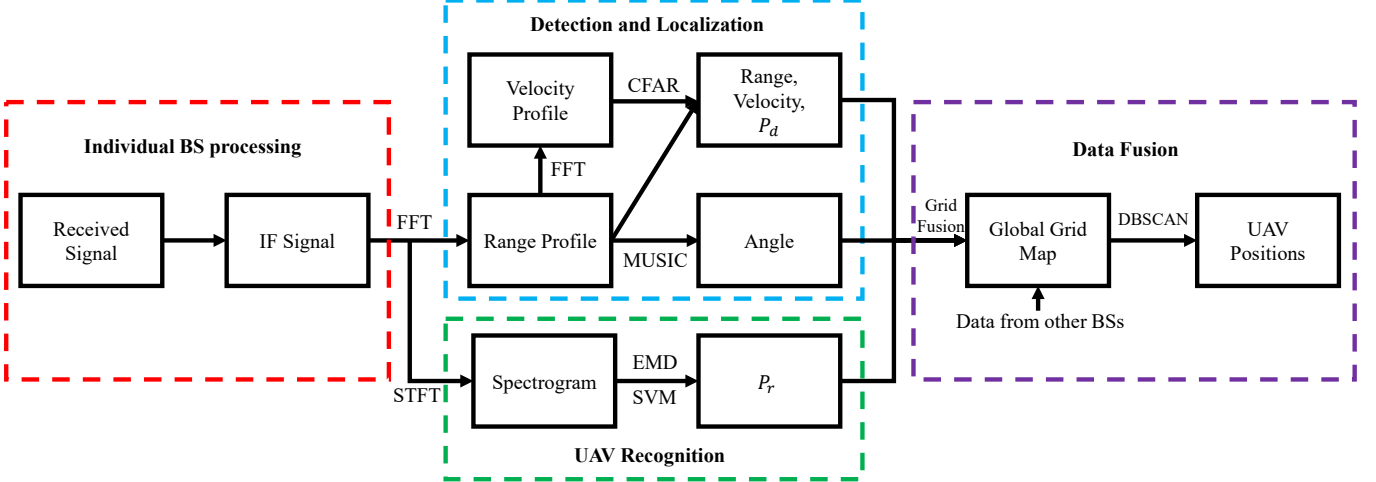


Fig. 3. The end-to-end framework for multi-BS collaborative UAV detection and localization.

(SNR) at the receiver. For the signal reflected from the direct path, the SNR is expressed as

$$\gamma_t = \frac{P_t}{N_0} = \frac{P_{tx}G_{tx}}{4\pi R^2} \cdot \sigma_t \cdot \frac{1}{4\pi R^2} \cdot \frac{G_{rx}\lambda^2}{4\pi} \cdot \frac{1}{N_0}, \quad (5)$$

where P_t is the input power of signal from target UAV, N_0 is the noise power, P_{tx} is the output power from the transmitter, R is the distance from the BS to the UAV, λ is the BS wavelength, σ_t is the non-fluctuating RCS of the UAV, and G_{tx} and G_{rx} are the antenna gains of the transmitter and receiver, respectively.

Conversely, the power of a signal received from an indirect path is lower than direct path due to the additional path loss and reflection losses. We typically only consider first-order ghosts, as higher-order ghosts have significantly lower energy. Assuming the distances from the reflector to the UAV and the BS are R_1 and R_2 respectively, and the RCS of the reflector is σ_r . Therefore, the SNR for an indirect path ghost can be expressed as

$$\gamma_g = \frac{P_{tx}G_{tx}}{4\pi R^2} \cdot \sigma_t \sigma_r \cdot \frac{1}{4\pi^2 R_1^2 R_2^2} \cdot \frac{G_{rx}\lambda^2}{4\pi} \cdot \frac{1}{N_0}. \quad (6)$$

III. UAV DETECTION AND LOCALIZATION ALGORITHM

This section introduces the comprehensive process of our proposed UAV Detection and Localization framework, where the parameter estimation, MDS extraction, multi-station data fusion, are elaborated, respectively. The end-to-end workflow is illustrated in Fig. 3.

A. Range, velocity and angle estimation

In this paper, we utilize the Linear Frequency Modulated Continuous Wave (LFMCW) as the transmitted signal $S(t)$, whose generation is compatible with the hardware capabilities of future BS, and is expressed as

$$S(t) = A \exp \{j2\pi (f_0 t + \mu t^2/2)\}, \quad (7)$$

where f_0 is the carrier frequency, $\mu = B/T$ is the linear modulation slope for a signal with bandwidth B and duration T , and A is the amplitude. At each BS, the range, angle, and velocity of UAV are obtained from the received echoes through following signal processing steps.

1) *Intermediate Frequency (IF) Signal Generation*: The IF signal is achieved by mixing the received echoes in (1) with a local copy of the transmitted signal. This process, known as de-chirping, shifts the echoes from different scatterers to baseband, where each scatterer's echo becomes a sinusoidal tone. The resulting baseband IF signal $r_{IF}(t)$ is written as

$$r_{IF}(t) = \sum_{i=0}^{N_t} A_i S_{IF_i}(t - \tau_i(t)) + \sum_{j=N_t+1}^{N_t+N_g+1} A_j S_{IF_j}(t - \tau_j(t)) + \tilde{w}(t), \quad (8)$$

where $S_{IF_i}(t)$ represents the IF component corresponding to the i -th scatterer, and $\tilde{w}(t)$ is the mixer noise. The frequency of each IF component $S_{IF_i}(t)$ is proportional to the round-trip delay $\tau_i(t)$, which in turn encodes its range and velocity.

2) *IF Signal Digitalization*: The analog IF signal is then sampled to produce a discrete-time signal. Denoting sampling period as $T_s = T/L$, the sampling time is $t = mT + lT/L$, where $l \in \{0, \dots, L-1\}$ and $m \in \{0, \dots, M-1\}$ represent the fast-time (for range) and slow-time (for velocity) domains, respectively. The discrete received signal is expressed as

$$s_r(l, m) = r_{IF}(mT + lT/L) + \tilde{w}(mT + lT/L). \quad (9)$$

This forms a matrix $\mathbf{S}_r \in \mathbb{R}^{L \times M}$.

3) *Range Profile Generation*: A range profile is generated by performing a Fast Fourier Transform (FFT) along the fast-time domain. A Hamming window is typically applied before the FFT to reduce sidelobes, which means the rang matrix

$$\mathbf{R} = (\mathbf{W}_L \mathbf{F}_L) \cdot \mathbf{S}_r \in \mathbb{R}^{L \times M}, \quad (10)$$

where \mathbf{W}_L is the windowing matrix and \mathbf{F}_L is the FFT matrix. Therefore, the range corresponding to the l -th bin is estimated as

$$R(l) = \frac{c f_s l}{2 L \mu}, \quad (11)$$

where $f_s = 1/T_s$ is the sampling frequency.

4) *Velocity Profile Generation*: Similarly, a velocity profile is obtained by performing an FFT across the slow-time

domain, and is expressed as

$$\mathbf{V} = \mathbf{R} \cdot (\mathbf{W}_M \mathbf{F}_M) \in \Re^{L \times M}. \quad (12)$$

The velocity corresponding to the m -th bin is estimated as

$$V(m) = \frac{cm}{2f_0MT}. \quad (13)$$

5) *Range and Velocity Determination*: Subsequently, a CA-CFAR detection strategy is adopted to distinguish UAV echoes from background noise in the range-velocity map [88]. The main steps are listed in Algorithm 1. A closed-form of the detection probability, $P_{d,t}$ for a specific UAV/ghost, can be achieved by calculating the probability that the signal envelope is over the detection threshold [89] as

$$P_{d,t} = \left(1 + \frac{(N_R N_V) (P_{FA}^{-1/(N_R N_V)} - 1)}{(N_R N_V) (1 + \gamma_t)} \right)^{-N_R N_V}, \quad (14)$$

where P_{FA} is the desired false alarm rate, and N_R and N_V are the number of reference cells in range and velocity.

Algorithm 1 The CFAR-based range and velocity estimation

- 1: **Initialization:** Determine the false alarm probability P_{FA} , the number of reference units N_R in range and N_V in velocity, set estimation index $q = 0$.
- 2: **for** $l = 0 : L - 1, m = 0 : M - 1$ **do**
- 3: Compute the mean signal power $\beta_{l,m}$ within the reference windows.
- 4: Determine the threshold γ_{th} using $\gamma_{th} = (N_R \cdot N_V) (P_{FA}^{-1/(N_R \cdot N_V)} - 1) \beta_{l,m}$.
- 5: **if** the power of detection unit $E_{l,m} \geq \gamma_{th}$ **then**
- 6: $\hat{R}(q) = R(l), \hat{V}(q) = V(m)$.
- 7: $q = q + 1$.
- 8: **end if**
- 9: **end for**
- 10: **Output:** $\hat{\mathbf{R}}, \hat{\mathbf{V}}$.

6) *Angle Estimation*: As established in the signal model, each BS is equipped with a ULA, allowing it to estimate the AoA of the signals reflected from a UAV. Off-the-shelf estimator as multiple signal classification (MUSIC) [90] can be used. The angle estimates for these two algorithms are expressed as

$$\hat{\theta}_{\text{MUSIC}} = \arg \min_{\theta} \mathbf{a}(\theta)^H \mathbf{U}_N \mathbf{U}_N^H \mathbf{a}(\theta), \quad (15)$$

where \mathbf{U}_N is the noise subspace matrix and $\mathbf{a}(\theta)$ is the array steering vector. These estimated parameters including range, velocity, angle, and detection probability are then available for multi-BS fusion and further analysis.

B. Micro-Doppler Feature Enhancement for UAV Recognition

While the CA-CFAR detector can identify the presence of moving objects, it cannot distinguish a UAV from other objects. To achieve robust UAV recognition, we leverage the unique MDS generated by the rotating blades of a UAV. These micro-motions produce a distinct frequency modulation on

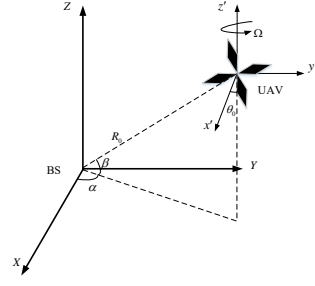


Fig. 4. Geometric model for analyzing the micro-Doppler effect from a UAV's rotor blade as observed by a BS.

the reflected echo signal, which can be used as a feature for classification [91]. To model this effect, we consider a UAV with N_{rot} rotors. The echoes from a single rotor can be modeled as the coherent sum of reflections from its N_{bl} blades [92], [93]. The echo from one rotor $s_{n_{\text{rot}}}(t)$ can be expressed as

$$s_{n_{\text{rot}}}(t) = L_{\text{bl}} e^{-j \frac{4\pi}{\lambda} R_0} \sum_{n_{\text{bl}}=0}^{N_{\text{bl}}-1} \text{sinc}\left\{\frac{2\pi L_{\text{bl}}}{\lambda} \cos \beta \cos(\theta_{n_{\text{bl}}} + \Omega t - \alpha)\right\} e^{-j \Phi_{n_{\text{bl}}}(t)}, \quad (16)$$

where L_{bl} is the length of a single blade. As shown in Fig. 4, R_0 is the distance from the rotor's center of rotation to the BS, Ω is the rotational angular frequency of the blade, and α and β are the azimuth and elevation angles of the rotor relative to the BS line-of-sight (LoS), respectively. The term $\Phi_{n_{\text{bl}}}(t)$ represents the phase function of the n_{bl} -th blade. The total echo signal from the UAV $S_{\Sigma}(t)$ is the sum of echoes from all its rotors,

$$S_{\Sigma}(t) = \sum_{n_{\text{rot}}=1}^{N_{\text{rot}}} s_{n_{\text{rot}}}(t). \quad (17)$$

To classify the UAV based on this signal, we employ a process involving EMD and a SVM classifier. The full procedure for acquiring the recognition probability P_r is described in Algorithm 2. A STFT is first applied to $S_{\Sigma}(t)$ to generate a time-frequency spectrogram to represent the MDS. The EMD algorithm then decomposes the signal into a set of intrinsic mode functions (IMFs). Features such as zero-crossing rate, normalized energy, and standard deviation are extracted from the first four IMFs. These features form a vector that is fed into a pre-trained SVM classifier, which outputs the recognition probability P_r . This probability quantifies the confidence that the detected object is indeed a UAV.

C. Multi-Station Data Fusion for Localization

While a single BS can estimate the range, velocity, and angle of a UAV, its observations are susceptible to errors from noise, clutter, and multipath ghosts. To overcome these limitations and achieve robust, high-accuracy localization, we fuse observations from multiple spatially BSs. A grid-based probabilistic data fusion framework is proposed to reduce interference and enhances the reliability of the final localization.

Algorithm 2 Recognition Probability Acquisition

- 1: **Input:** Total echo signal from t -th UAV, S_Σ .
- 2: **Step 1:** Convert the echo signal to a real signal $x_\Sigma = |S_\Sigma| \in \mathbb{R}$.
- 3: **Step 2:** Decompose x_Σ into $x_\Sigma = \sum_{d=1}^D m_d + q_D$ using the EMD algorithm, where m_d is the d -th Intrinsic Mode Function (IMF) and q_D is the residual.
- 4: **Step 3:** Extract features (zero-crossing number, normalized signal energy, standard deviation, and zero-crossing ratio) from the first four IMFs.
- 5: **Step 4:** Obtain the recognition probability $P_{r,t}$ by feeding the feature vector into an SVM classifier with a radial basis function (RBF) kernel.
- 6: **Output:** Recognition probability, $P_{r,t}$.

The process involves grid initialization and calibration, data fusion, and clustering.

1) *Grid Initialization and Calibration:* The first step is to discretize the surveillance area into a grid and to map the local observations from each BS into this common, unified world coordinate system. This ensures that all measurements can be compared and combined meaningfully.

A critical aspect of this process is determining the size of the grid cells, which should be related to the resolution of the sensing BSs. For a given BS, a measurement corresponds not to an infinitesimal point but to a “possible detection region”, the size of which is determined by its range and angular resolution. As shown in Fig. 5, the size of this region h_n for the n -th BS is the minimum of its effective range and beam resolutions with

$$h_n = \min\{h_{n,\text{range}}, h_{n,\text{beam}}\}, \quad (18)$$

where $h_{n,\text{range}}$ and $h_{n,\text{beam}}$ are defined as:

$$h_{n,\text{range}} = \underbrace{\Delta R}_{\text{range resolution}} / \cos \varsigma_n = \frac{c}{2B} / \cos \varsigma_n, \quad (19)$$

$$h_{n,\text{beam}} = r_n \underbrace{\vartheta_{n,3}}_{\text{angle resolution}} / \sin \varsigma_n. \quad (20)$$

Here, ΔR is the intrinsic range resolution (dependent on bandwidth), and $\vartheta_{n,3}$ is the 3dB beamwidth of the antenna, and r_n is the measured range, and ς_n is the transmission angle. The final grid size for the entire map is chosen to be the minimum resolution across all participating BSs to avoid loss of information.

Once the grid is established, each local measurement is calibrated. Let the position of the n -th BS in the world be $\mathbf{x}_n = (x_n, y_n)$, with a rotation angle ψ_n . If this BS detects a UAV at range r_n and angle θ_n , the UAV’s world position, \mathbf{x}_{tn} , is calculated as

$$\begin{bmatrix} x_{tn} \\ y_{tn} \end{bmatrix} = \begin{bmatrix} x_n \\ y_n \end{bmatrix} + r_n \begin{bmatrix} \cos(\psi_n + \theta_n) \\ \sin(\psi_n + \theta_n) \end{bmatrix}. \quad (21)$$

This mapping allows us to translate every detection from its local polar coordinates to the corresponding grid cells in the global map.

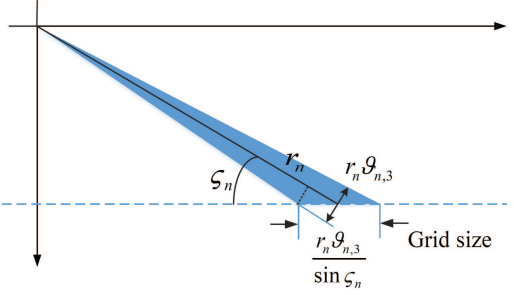


Fig. 5. Determination of the possible detection region.

2) *Data Fusion on a Grid Map:* After calibration, the observations are fused on the grid map. This probabilistic approach combines information while filtering out inconsistent measurements, such as those from ghosts.

The event that grid cell i is occupied by a UAV is defined as O_i . When the n -th BS receives an echo that maps to grid cell i (event $y_i^{(n)}$), the posterior probability of the cell being occupied is updated using the Bayesian theorem as

$$p(O_i|y_i^{(n)}) = p(O_i) \cdot p(y_i^{(n)}|O_i). \quad (22)$$

The likelihood term $p(y_i^{(n)}|O_i)$ is the recognition probability P_r from the micro-Doppler analysis. This assigns higher likelihood to detections that exhibit UAV-like characteristics, effectively suppressing echoes from unintentional objects.

To combine observations from all N_{BS} BSs, we adopt a log-likelihood ratio probability fusion framework. For the n -th BS, the occurrence probability of grid cell i is updated iteratively

$$p(O_i)^{(n)} = \log\left(\frac{p(O_i|y_i^{(n)})}{P_{\text{FA}}}\right) + p(O_i)^{(n-1)}. \quad (23)$$

After iterating through all BSs, the final fused grid map contains enhanced probabilities for true UAV locations. The complete process is detailed in Algorithm 3. The final UAV position, $\hat{\mathbf{p}}$, can then be estimated using a minimum mean square error (MMSE) as

$$\hat{\mathbf{p}} = \sum_{i=1}^{N_t} p(O_i)^{(N_{\text{BS}})} l_i, \quad (24)$$

where l_i is the location of the i -th grid cell.

3) *Clustering for Multiple UAVs:* In scenarios with multiple UAVs, the fused grid map may contain several high-probability regions. To distinguish individual UAVs, we use the Density-Based Spatial Clustering of Applications with Noise (DBSCAN) method. DBSCAN groups high-probability grid cells into distinct clusters, each corresponding to a different UAV while identifying sparse noise points [94]. The algorithm is detailed in Algorithm 4.

IV. PERFORMANCE ANALYSIS AND OPTIMIZATION

A. The Cramer-Rao Lower Bound

To evaluate the fundamental performance limits of the proposed multi-BS localization system, we utilize the CRLB, which provides a theoretical lower bound on the MSE for any unbiased estimator of a UAV’s position. According to

Algorithm 3 Grid Map Based Multi-BS Fusion

- 1: **Initialization:** Number of BSs N_{BS} , grid point locations l_i , BS locations and orientations \mathbf{x}_n, ψ_n , and initial probabilities $p(O_i)$.
- 2: **for** BS $n = 1 : N_{\text{BS}}$ **do**
- 3: For each local measurement (r_n, θ_n) , determine the possible detection region \mathbf{R} on the grid map.
- 4: **for** each grid point $i \in \mathbf{R}$ **do**
- 5: $p(O_i)^{(n)} = \log\left(\frac{p(O_i|y_i^{(n)})}{P_{\text{FA}}}\right) + p(O_i)^{(n-1)}$
- 6: **end for**
- 7: **end for**
- 8: **Normalization:** Normalize the final probabilities across the grid.
- 9: **Output:** MMSE-based position estimate $\hat{\mathbf{p}}$.

Algorithm 4 Clustering using DBSCAN

- 1: **Initialization:** The fused localization map \mathbf{M} , the radius of the Epsilon area (Eps), and the minimum number of neighbors (N_{Pts}).
- 2: **for** each point \mathbf{P} in \mathbf{M} not yet visited **do**
- 3: Mark \mathbf{P} as visited.
- 4: Find all neighbor points of \mathbf{P} within Eps.
- 5: **if** the number of neighbors is less than N_{Pts} **then**
- 6: Mark \mathbf{P} as noise.
- 7: **else**
- 8: Create a new cluster C and add \mathbf{P} to it.
- 9: For each neighbor point \mathbf{P}' of \mathbf{P} :
- 10: If \mathbf{P}' is not visited, mark it as visited and find its neighbors. If it has enough neighbors, add them to a queue to be processed.
- 11: If \mathbf{P}' is not yet a member of any cluster, add \mathbf{P}' to cluster C .
- 12: **end if**
- 13: **end for**

the Fisher information inequality, the MSE of the position estimate, $\hat{\mathbf{p}}$, is bounded as follows

$$\mathbb{E}\{\|\hat{\mathbf{p}} - \mathbf{p}\|^2\} \geq \mathcal{P}(\mathbf{p}) = \text{tr}\{\mathbf{J}_e(\mathbf{p})^{-1}\}, \quad (25)$$

where $\mathbf{J}_e(\mathbf{p})$ is the equivalent Fisher information matrix (EFIM) for the entire system [95]. The EFIM is constructed by aggregating the information from each antenna element of every participating BS. We can state the following proposition regarding its structure.

Proposition 1: If there are N_{BS} BSs deployed, and each BS is equipped with a K -element uniform linear antenna array, the equivalent EFIM of the UAV's position can be expressed as the sum of the individual information matrices from each antenna's ToA and AoA measurements:

$$\mathbf{J}_e(\mathbf{p}) = \sum_{n=1}^{N_{\text{BS}}} \sum_{k=1}^K (\mathbf{J}_{nk}^{\text{TOA}}(\mathbf{p}) + \mathbf{J}_{nk}^{\text{AOA}}(\mathbf{p})), \quad (26)$$

where $\mathbf{J}_{nk}^{\text{TOA}}(\mathbf{p})$ and $\mathbf{J}_{nk}^{\text{AOA}}(\mathbf{p})$ are the FIM for the ToA and DoA measurements, respectively, from the k -th antenna element of the n -th BS.

Proof: The detailed derivation of the Fisher Information Matrix is provided in the Appendix.

This proposition highlights two key remarks.

- At each individual BS, the measurement information obtained from ToA ($\mathbf{J}^{\text{TOA}}(\mathbf{p})$) and DoA ($\mathbf{J}^{\text{AOA}}(\mathbf{p})$) can be linearly accumulated. The quality of this information is determined by system parameters such as transmit power and signal bandwidth, as well as the geometric relationship between the BS and the UAV.
- The measurement information from multiple BSs can also be linearly accumulated. This demonstrates that observations from all N_{BS} BSs can be combined to achieve a more accurate and reliable position estimate compared to what is possible with a single BS.

The CRLB serves as an essential performance benchmark, allowing us to quantify how close the accuracy of our proposed fusion and localization algorithms comes to the theoretical best-case scenario.

B. Reinforcement Learning for Station Selection

In a dense network of BSs, it is often inefficient and unnecessary to activate all of them for UAV detection. Activating only the most useful BSs can significantly reduce energy consumption and computational load while maintaining or even improving localization accuracy. This section formulates the BS selection task as an optimization problem and presents a RL-based solution. We first consider a single UAV scenario and then extend the framework to handle multiple UAVs.

1) Single UAV Scene:

a) Problem Formulation: For a single UAV scene with a total of N_{BS} available BSs, our objective is to select a subset of these BSs to find a balance between minimizing the localization MSE and the resource cost (number of active BSs). With the true position of the UAV being \mathbf{p}_t and the estimated position being $\hat{\mathbf{p}}_t$, the MSE is $\mathcal{M}(\mathbf{R}, \mathbf{p}_t)$. The optimization problem can then be written as

$$\begin{aligned} \mathcal{P}_1: \min & \quad \tau_e \mathcal{M}(\mathbf{R}, \mathbf{p}_t) + \tau_r R_s \\ \text{s.t.} & \quad \mathbf{R} = \{r_1, r_2, \dots, r_{N_{\text{BS}}}\}, \\ & \quad r_n \in \{0, 1\}, \end{aligned} \quad (27)$$

where \mathbf{R} is the selection vector, with $r_n = 1$ indicating that the n -th BS is selected. R_s is the total number of selected BSs. τ_e and τ_r are the weighting factors for the MSE and resource cost, respectively. Since the MSE cannot be easily formulated as a closed-form function of the BS selection state \mathbf{R} , we adopt a non-parametric, model-free learning strategy.

b) Node Selection Strategy: We employ Q-learning to find an optimal policy for BS selection. The Q-learning framework is defined within a Markov Decision Process (MDP) as follows:

- **Agent:** The agent is the BS sensor network responsible for positioning.
- **State:** The state is the power allocation status for all BSs, represented by a binary vector \mathbf{R} indicating which BSs are currently active (on/off).

- **Action:** An action is the decision to change the state, i.e., to select a new subset of BSs to activate for the next measurement.
- **Environment:** The environment is the physical space containing the UAV. The agent's interaction with the environment yields an observation, which is the localization result obtained using the fusion framework from the previously selected BSs.

The Q-learning algorithm iteratively updates a Q-table, which estimates the long-term reward of taking a certain action from a given state. The agent explores different selection strategies using an ϵ -greedy policy. The reward function is designed to reflect the objective function \mathcal{P}_1

$$r = C_0 - \tau^e \mathcal{M} - \tau^r R_s, \quad (28)$$

where C_0 is a constant baseline reward. By maximizing this reward, the agent learns to select BS configurations that result in a good trade-off between positioning error and resource cost. The complete training and regression process is outlined in Algorithm 5. To improve real-time performance, a pre-trained Back Propagation (BP) neural network can be used to approximate the Q-function, enabling rapid selection of the sub-optimal action based on a coarse initial UAV position estimate.

Algorithm 5 Reinforcement Learning Based BS Selection

- 1: **Initialization:**
- 2: A sensor network with N_{BS} BSs with locations $\mathbf{p}_1, \mathbf{p}_2, \dots, \mathbf{p}_{N_{BS}}$ and one single UAV with location \mathbf{p}_t . The estimated position of the UAV is $\hat{\mathbf{p}}_t$ according to Algorithm 3.
- 3: Generate the training dataset with N_{train} UAV positions, expressed as $N_{train} = 1, 2, \dots, N_{train}$.
- 4: Define the RL values: i) State S , a binary series representing the on-off of BS nodes. ii) Reward r , affected by the localization error and number of enabled nodes. iii) Action A , the selection or abandonment of BS nodes.
- 5: **Training:**
- 6: **repeat**
- 7: Initialize the Q-table.
- 8: **for** each episode of Q-learning **do**
- 9: **if** current iteration \leq upper limit **then**
- 10: Select a set of actions with an ϵ -greedy policy.
- 11: Update the Q-table and current state.
- 12: **end if**
- 13: **end for**
- 14: **until** all N_{train} data are processed
- 15: **Regression:**
- 16: Input the coarse estimated UAV position $\hat{\mathbf{p}}_{tc}$.
- 17: Derive the sub-optimal action with the pre-trained BP network: $\hat{A} = \text{BP network}(\hat{\mathbf{p}}_{tc})$.

2) Multi-UAV Scene:

a) *General Extension:* When multiple UAVs are present, the objective function is modified to account for the localization error of all M UAVs. The optimization problem, \mathcal{P}_2 ,

becomes minimizing the sum of weighted MSEs and the resource cost

$$\begin{aligned} \mathcal{P}_2: \min & \sum_{m=1}^M \tau_e \mathcal{M}_m(\mathbf{R}, \mathbf{p}_t) + \tau_r R_s \\ \text{s.t.} & \mathbf{R} = \{r_1, r_2, \dots, r_{N_{BS}}\}, \\ & r_n \in \{0, 1\}. \end{aligned} \quad (29)$$

To satisfy this requirement, the reward function in the Q-learning algorithm must be adjusted to reflect this new objective.

b) *Suboptimal Scheme:* Optimizing for multiple UAVs simultaneously can be complex. A practical, suboptimal approach is to define states based on localization performance. As shown in Fig. 6, we can define a finite number of states based on the distribution of the Root Mean Square Error (RMSE) using a clustering method like Fuzzy C-Means (FCM). The agent learns to select actions that move the system from poor states (e.g., S1) to good states (e.g., S5). The RL agent's goal is then to take actions that transition the system from a high-error state to a low-error state.

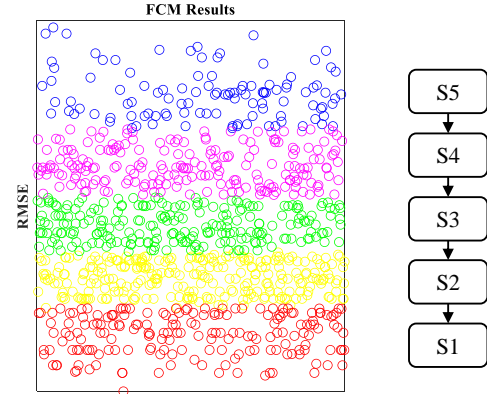


Fig. 6. States using FCM clustering on the RMSE distribution.

The problem can be reformulated to find the minimum number of BSs, R_s , that can achieve a localization MSE below a certain threshold, \mathcal{M}_{\max} , for all detected UAVs

$$\begin{aligned} \mathcal{P}_3: \min & R_s \\ \text{s.t.} & \mathcal{M}_m(\mathbf{R}, \mathbf{p}_t) < \mathcal{M}_{\max} \text{ for all } m = 1 \dots M. \end{aligned} \quad (30)$$

The Q-learning algorithm is then trained to satisfy this constraint. The state transitions from poor localization (high error) to accurate localization (error below \mathcal{M}_{\max}), and the algorithm stops when the error constraint is met, yielding an efficient BS selection.

V. EXPERIMENTAL AND SIMULATION RESULTS

A. Numerical Simulations

To validate the performance of the proposed framework, we conduct a series of numerical simulations. We first describe the simulation setup and then present the results for collaborative localization and reinforcement learning-based BS selection.

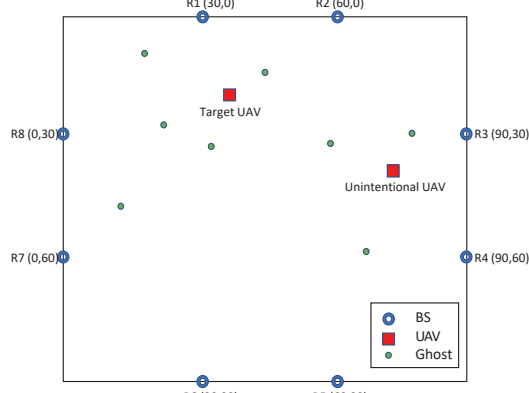


Fig. 7. The simulation deployment.

1) *Simulation Settings*: As shown in Fig. 7, the simulation environment consists of a $90\text{m} \times 90\text{m}$ area with a grid resolution of 0.1m . Two UAVs with different micro-Doppler characteristics are randomly located: “target UAV” (e.g., a quadcopter) and an “unintentional UAV” (e.g., a larger, helicopter-like UAV). 8 BSs are deployed at the edges of the map, each separated by 30m . All BSs are assumed to be synchronized.

To simulate a complex environment, reflectors are randomly distributed according to a Poisson Point Process (PPP) with an expectation of 3, which generate multipath ghost echoes. The key simulation parameters for the BSs are listed in Tab. I.

TABLE I: BS Simulation Parameters

Parameter	Value	Parameter	Value
Carrier Frequency (f_0)	24 GHz	Bandwidth (B)	100 MHz
Pulse Duration (T)	1 ms	Samples (L)	128
Number of Pulses (M)	64	P_{FA}	0.001

2) *Localization Results*: The simulated localization process is presented in Fig. 8, where the color map represents the detection probability. The process demonstrates the progressive refinement from raw single-BS data to a precise, fused localization result.

a) *Single BS Detection*: Initially, we evaluate the performance of a single BS (located at R1 in Fig. 7). As shown in Fig. 8 (a), the single BS generates a probabilistic map containing multiple potential detections. It is unable to distinguish the true UAVs from the multipath ghosts, highlighting the challenge of localization in complex environments.

b) *Observations from Multiple BSs*: Next, we apply the proposed data fusion framework to combine observations from all eight BSs. By comparing Fig. 8 (a) and Fig. 8(b), it is clear that the fusion process significantly enhances the detection probabilities at the true UAV locations while suppressing the probabilities of the inconsistent ghost detections. By applying a threshold (set to half the peak probability value), the influence of multipath reflections is almost entirely mitigated, as shown in Fig. 8(c). Finally, by applying the DBSCAN clustering and micro-Doppler recognition algorithms, the target of interest is successfully isolated and localized, as shown in Fig. 8 (d).

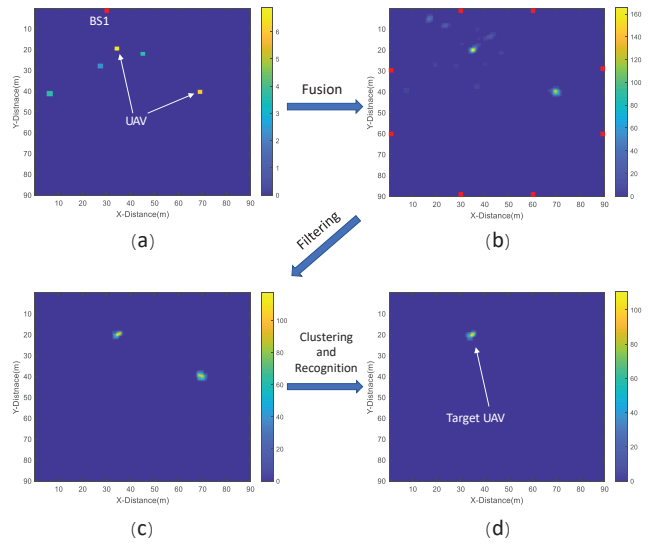


Fig. 8. The step-by-step target positioning process.

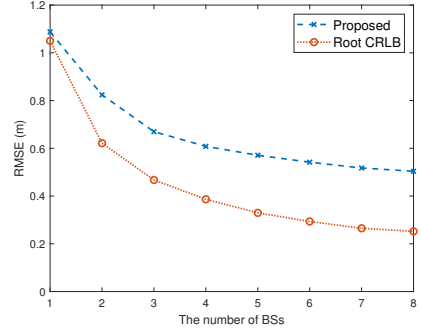


Fig. 9. MSE versus the number of active BSs.

c) *Performance Analysis*: To quantitatively assess the performance, we conducted 5000 Monte Carlo simulations. Fig. 9 shows the mean positioning error (MMSE) as a function of the number of active BSs, compared against the theoretical CRLB. The results clearly show that the localization error decreases as more BSs are used, demonstrating the benefit of collaborative sensing. The cumulative distribution function (CDF) of the positioning error, shown in Fig. 10, further illustrates that using all eight BSs provides a significant improvement over using a single or a small number of BSs.

3) *Node Selection Results*: We now evaluate the performance of the reinforcement learning-based BS selection algorithms, considering both the single-UAV objective (\mathcal{P}_1) and the multi-UAV objective (\mathcal{P}_2). We performed 2000 training iterations followed by 2000 Monte Carlo simulations, varying the number of UAVs from one to six.

a) *RMSE Performance*: Fig. 11 shows the total localization error versus the number of UAVs for three cases: using all BSs, using the \mathcal{P}_1 optimization, and using the \mathcal{P}_2 optimization. Both optimization methods outperform the baseline of using all BSs. The \mathcal{P}_1 method achieves the lowest error, while the \mathcal{P}_2 method still offers a significant improvement of nearly 0.4 meters over the baseline. The CDF

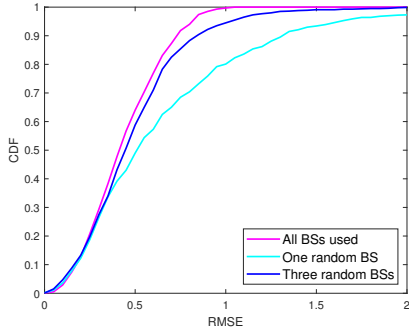


Fig. 10. CDF of the positioning error.

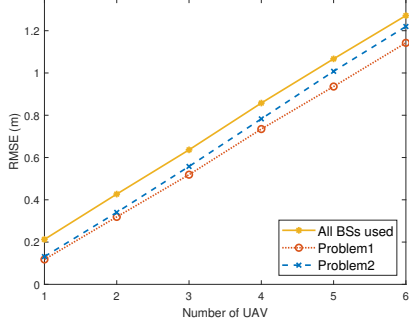


Fig. 11. Positioning error versus the number of UAVs.

of the localization error for a three-UAV scenario is shown in Fig. 12, confirming that both optimization methods yield better performance than the baseline, though they remain above the theoretical lower bound due to the inclusion of resource cost in the reward function.

B. Practical Experiments

In addition to simulations, we conducted practical experiments to validate the proposed framework in a real-world indoor environment. The experiments demonstrate the effectiveness of both the micro-Doppler based UAV recognition and the multi-BS data fusion for improving localization accuracy.

1) *Experimental Setup*: The experiments were carried out using a K-band (24 GHz) FMCW radar kit (Ancortek SDR-kit 2400AD2), as shown in Fig. 13(a). The radar is capable of generating the necessary waveforms for sensing and is equipped with one transmit and two receive horn antennas, allowing for both ToA and AoA measurements as described in Section IV-A.

The experimental scene, depicted in Fig. 13(b), was set up in a cluttered indoor environment containing various stationary objects like chairs and desks. Two distinct objects were used for the experiment: a target of interest, represented by an electric fan to emulate the rotating blades of a UAV, and an unintentional object, a stationary iron box.

To simulate a multi-BS scenario, the radar was placed at three different locations sequentially. The data from each location was recorded and then processed as if it were collected simultaneously from three separate, spatially distributed BSs.

2) *Micro-Doppler Characterization*: First, we analyzed the micro-Doppler signatures of the fan (UAV) and the iron box

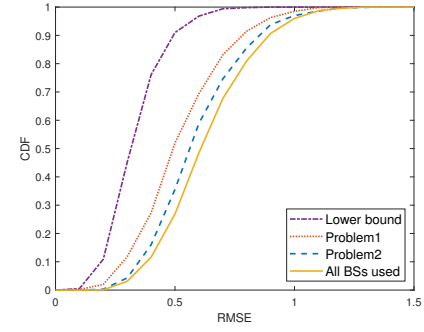


Fig. 12. CDF of the positioning error for a three-UAV scenario.

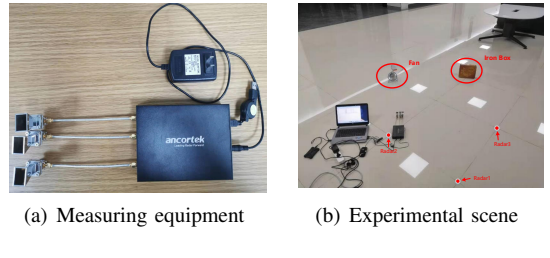


Fig. 13. Settings of practical experiment.

to verify the recognition capability of our system. Figure. 14 shows the time-frequency spectrograms for both objects.

A clear difference is visible: the fan's rotating blades produce a distinct periodic micro-Doppler signature, whereas the iron box, being stationary, exhibits no such features. We applied the EMD-SVM classifier described in Section IV-B to these signals. The resulting recognition probabilities (P_r) are shown in Tab. II. The classifier correctly identifies the fan as a UAV with high probability (0.8 to 0.93) across all three BS locations, while assigning a very low probability to the iron box. This confirms that the proposed feature enhancement method can effectively distinguish UAVs from other static or unintentional objects.

TABLE II: Experimental Target Recognition Probability (P_r)

Object \ BS	BS 1	BS 2	BS 3
Fan (UAV)	0.8	0.8667	0.9333
Iron Box	0.2667	0	0.2

3) *Multi-BS Fusion and Localization*: Next, we evaluated the performance of the multi-BS data fusion framework. Figure 15(a) shows the fused detection map using the basic detection probability (P_d) from all three BS locations. While both the fan (target of interest) and the iron box (unintentional target) are detected, the map is noisy.

Figure 15(b) shows the result after applying our complete framework, where the fusion is weighted by the recognition probability (P_r). The framework successfully suppresses the detection of the iron box and isolates the fan, providing a clean and unambiguous localization of the UAV.

The positioning errors for individual BSs and various fused combinations are listed in Tab. III. The results show that fusing observations from multiple BSs provides a more "balanced"

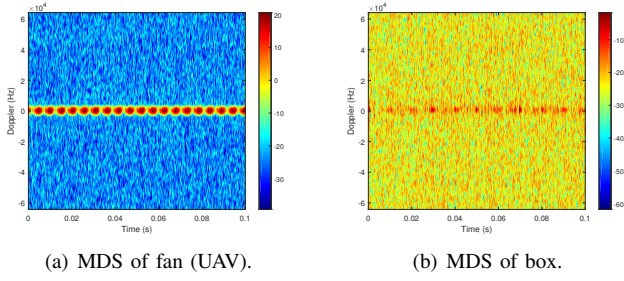


Fig. 14. Experimental micro-Doppler spectrograms.

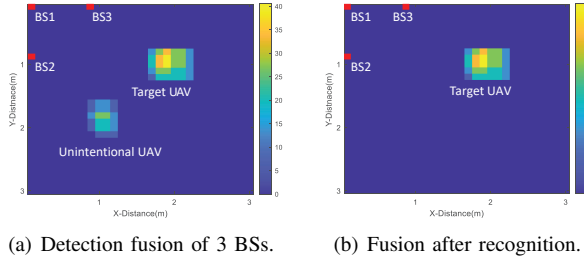


Fig. 15. Experimental fusion results.

and often more accurate solution. For instance, while BS 2 has the lowest individual error, BS 1 and BS 3 have significant errors. Fusing all three BSs yields a final error of 0.0627 m, which is a substantial improvement over the average individual performance. This demonstrates that multi-BS observations provide spatial diversity that effectively mitigates multipath effects and improves overall detection accuracy and reliability.

TABLE III: Positioning Error of Experiments

BS Configuration	Error (m)	Error	Mean
BS 1	0.0333		
BS 2	0.1414	0.1249	
BS 3	0.2000		
BS 1 and 2	0.0505		
BS 1 and 3	0.0514	0.0836	
BS 2 and 3	0.1490		
All three BSs	0.0627		

VI. CONCLUSION

In this paper, we investigated UAV sensing, detection and localization in the context of the emerging low-altitude economy, where the proliferation of LSS UAVs poses significant safety challenges. To address the limitations of conventional solutions, we proposed an RF-based cooperative sensing framework that leverages existing base stations, integrating CA-CFAR and MDS-based methods for robust UAV detection and recognition. A grid-based probabilistic data fusion and clustering strategy was introduced to mitigate ghost targets and improve multi-UAV localization accuracy. Furthermore, CRLB analysis and RL-based optimization were employed to balance localization performance and system efficiency. The feasibility and superiority of the proposed framework

are verified through both numerical simulations and practical experiments. Our method is shown to reduce localization error by over 40% through multi-station fusion, a result confirmed by experiments achieving centimeter-level accuracy, while our RL-based optimization efficiently manages network resources. Future work will extend the framework to more complex communication scenario and explore the co-design strategies between sensing and communication for large-scale UAV networks.

APPENDIX: PROOF OF PROPOSITION 1

The measurement equation for the position of a UAV, $\mathbf{p} = [x, y]^T$, as observed by N_{BS} BSs, each with K antennas, is given by the vector of observations \mathbf{Z} :

$$\mathbf{Z} = \begin{bmatrix} r_{11} \\ \theta_{11} \\ \vdots \\ r_{nk} \\ \theta_{nk} \\ \vdots \\ r_{N_{\text{BS}}K} \\ \theta_{N_{\text{BS}}K} \end{bmatrix} = \begin{bmatrix} f_r(\mathbf{p}_{11}) \\ f_\theta(\mathbf{p}_{11}) \\ \vdots \\ f_r(\mathbf{p}_{nk}) \\ f_\theta(\mathbf{p}_{nk}) \\ \vdots \\ f_r(\mathbf{p}_{N_{\text{BS}}K}) \\ f_\theta(\mathbf{p}_{N_{\text{BS}}K}) \end{bmatrix} + \mathbf{n} = \mathbf{H}(\mathbf{p}) + \mathbf{n} \quad (31)$$

where r_{nk} and θ_{nk} are the measured range and angle. The true range and angle, f_r and f_θ , are functions of the UAV's position \mathbf{p} and the antenna's position $\mathbf{p}_{nk} = [x_{nk}, y_{nk}]^T$:

$$f_r(\mathbf{p}_{nk}) = \sqrt{(x_{nk} - x)^2 + (y_{nk} - y)^2} \quad (32)$$

$$f_\theta(\mathbf{p}_{nk}) = \arctan\left(\frac{y_{nk} - y}{x_{nk} - x}\right) \quad (33)$$

The measurement noise vector \mathbf{n} is zero-mean Gaussian with covariance $\mathbf{\Lambda}$. The likelihood function is:

$$\rho(\mathbf{Z}; \mathbf{p}) = C \cdot \exp\left\{-\frac{1}{2} \sum_{n=1}^{N_{\text{BS}}} \sum_{k=1}^K [\lambda_{nk}^{\text{TOA}}(\delta_{nk}^r)^2 + \lambda_{nk}^{\text{AOA}}(\delta_{nk}^\theta)^2]\right\} \quad (34)$$

where $\delta_{nk}^r = r_{nk} - f_r(\mathbf{p}_{nk})$ and $\delta_{nk}^\theta = \theta_{nk} - f_\theta(\mathbf{p}_{nk})$ are the measurement errors, and C represents the constant terms from the likelihood function's normalization factor, which will not influence the subsequent derivatives with respect to \mathbf{p} . The log-likelihood function is:

$$\ln \rho(\mathbf{Z}; \mathbf{p}) = \ln C - \frac{1}{2} \sum_{n=1}^{N_{\text{BS}}} \sum_{k=1}^K [\lambda_{nk}^{\text{TOA}}(\delta_{nk}^r)^2 + \lambda_{nk}^{\text{AOA}}(\delta_{nk}^\theta)^2] \quad (35)$$

The first-order partial derivative of the log-likelihood is:

$$\begin{aligned} \frac{\partial \ln \rho(\mathbf{Z}; \mathbf{p})}{\partial \mathbf{p}} = & \sum_{n=1}^{N_{\text{BS}}} \sum_{k=1}^K \left[\lambda_{nk}^{\text{TOA}}(\delta_{nk}^r) \frac{\partial f_r(\mathbf{p}_{nk})}{\partial \mathbf{p}} \right. \\ & \left. + \lambda_{nk}^{\text{AOA}}(\delta_{nk}^\theta) \frac{\partial f_\theta(\mathbf{p}_{nk})}{\partial \mathbf{p}} \right] \end{aligned} \quad (36)$$

The second-order partial derivative is:

$$\frac{\partial^2 \ln \rho(\mathbf{Z}; \mathbf{p})}{\partial \mathbf{p} \partial \mathbf{p}^T} = \sum_{n=1}^{N_{\text{BS}}} \sum_{k=1}^K [\lambda_{nk}^{\text{TOA}} \gamma_{r_{nk}} + \lambda_{nk}^{\text{AOA}} \gamma_{\theta_{nk}}] \quad (37)$$

where

$$\gamma_{r_{nk}} = -\frac{\partial f_r}{\partial \mathbf{p}} \left(\frac{\partial f_r}{\partial \mathbf{p}} \right)^T + (\delta_{nk}^r) \frac{\partial^2 f_r}{\partial \mathbf{p} \partial \mathbf{p}^T} \quad (38)$$

$$\gamma_{\theta_{nk}} = -\frac{\partial f_\theta}{\partial \mathbf{p}} \left(\frac{\partial f_\theta}{\partial \mathbf{p}} \right)^T + (\delta_{nk}^\theta) \frac{\partial^2 f_\theta}{\partial \mathbf{p} \partial \mathbf{p}^T} \quad (39)$$

The Fisher Information Matrix (FIM) is the negative expectation of the second-order derivative. Since the expectation of the error terms $E[\delta_{nk}^r]$ and $E[\delta_{nk}^\theta]$ is zero, the second terms in $\gamma_{r_{nk}}$ and $\gamma_{\theta_{nk}}$ vanish.

$$\begin{aligned} \mathbf{J}_e(\mathbf{p}) &= -E \left[\frac{\partial^2 \ln \rho(\mathbf{Z}; \mathbf{p})}{\partial \mathbf{p} \partial \mathbf{p}^T} \right] \\ &= E \left[\sum_{n=1}^{N_{BS}} \sum_{k=1}^K \left(\lambda_{nk}^{\text{TOA}} \frac{\partial f_r}{\partial \mathbf{p}} \frac{\partial f_r}{\partial \mathbf{p}^T} + \lambda_{nk}^{\text{AOA}} \frac{\partial f_\theta}{\partial \mathbf{p}} \frac{\partial f_\theta}{\partial \mathbf{p}^T} \right) \right] \end{aligned} \quad (40)$$

The partial derivatives of the range and angle functions are:

$$\frac{\partial f_r}{\partial \mathbf{p}} = \begin{bmatrix} -\cos \theta_{nk} \\ -\sin \theta_{nk} \end{bmatrix} = -\mathbf{q}_{nk}^{\text{TOA}} \quad (41)$$

$$\frac{\partial f_\theta}{\partial \mathbf{p}} = \frac{1}{f_r} \begin{bmatrix} \sin \theta_{nk} \\ -\cos \theta_{nk} \end{bmatrix} = \frac{1}{f_r} \mathbf{q}_{nk}^{\text{AOA}} \quad (42)$$

The outer product for the ToA component is:

$$\begin{aligned} \frac{\partial f_r}{\partial \mathbf{p}} \left(\frac{\partial f_r}{\partial \mathbf{p}} \right)^T &= \begin{bmatrix} -\cos \theta_{nk} \\ -\sin \theta_{nk} \end{bmatrix} [-\cos \theta_{nk} \ -\sin \theta_{nk}] \\ &= \begin{bmatrix} \cos^2 \theta_{nk} & \cos \theta_{nk} \sin \theta_{nk} \\ \cos \theta_{nk} \sin \theta_{nk} & \sin^2 \theta_{nk} \end{bmatrix} \\ &= \mathbf{q}_{nk}^{\text{TOA}} (\mathbf{q}_{nk}^{\text{TOA}})^T \end{aligned} \quad (43)$$

And the outer product for the AoA component is:

$$\begin{aligned} \frac{\partial f_\theta}{\partial \mathbf{p}} \left(\frac{\partial f_\theta}{\partial \mathbf{p}} \right)^T &= \frac{1}{f_r^2} \begin{bmatrix} \sin \theta_{nk} \\ -\cos \theta_{nk} \end{bmatrix} [\sin \theta_{nk} \ -\cos \theta_{nk}] \\ &= \frac{1}{f_r^2} \begin{bmatrix} \sin^2 \theta_{nk} & -\sin \theta_{nk} \cos \theta_{nk} \\ -\sin \theta_{nk} \cos \theta_{nk} & \cos^2 \theta_{nk} \end{bmatrix} \\ &= \frac{1}{f_r^2} \mathbf{q}_{nk}^{\text{AOA}} (\mathbf{q}_{nk}^{\text{AOA}})^T \end{aligned} \quad (44)$$

Substituting these results back into the FIM expression yields the final form:

$$\begin{aligned} \mathbf{J}_e(\mathbf{p}) &= \sum_{n=1}^{N_{BS}} \sum_{k=1}^K \left\{ \lambda_{nk}^{\text{TOA}} (\mathbf{q}_{nk}^{\text{TOA}}) (\mathbf{q}_{nk}^{\text{TOA}})^T \right. \\ &\quad \left. + \frac{\lambda_{nk}^{\text{AOA}}}{f_r^2} (\mathbf{q}_{nk}^{\text{AOA}}) (\mathbf{q}_{nk}^{\text{AOA}})^T \right\} \\ &= \sum_{n=1}^{N_{BS}} \sum_{k=1}^K \left(\mathbf{J}_{nk}^{\text{TOA}}(\mathbf{p}) + \mathbf{J}_{nk}^{\text{AOA}}(\mathbf{p}) \right) \end{aligned} \quad (45)$$

REFERENCES

- [1] H. Huang, J. Su, and F.-Y. Wang, "The potential of low-altitude airspace: The future of urban air transportation," *IEEE Transactions on Intelligent Vehicles*, 2024.
- [2] D. He, W. Yuan, J. Wu, and R. Liu, "Ubiquitous UAV communication enabled low-altitude economy: Applications, techniques, and 3gpp's efforts," *IEEE Network*, 2025.
- [3] Y. Ping, T. Liang, H. Ding, G. Lei, J. Wu, X. Zou, K. Shi, R. Shao, C. Zhang, W. Zhang *et al.*, "Multimodal large language models-enabled UAV swarm: Towards efficient and intelligent autonomous aerial systems," *arXiv preprint arXiv:2506.12710*, 2025.
- [4] Q. Wu, J. Xu, Y. Zeng, D. W. K. Ng, N. Al-Dhahir, R. Schober, and A. L. Swindlehurst, "A comprehensive overview on 5G-and-beyond networks with UAVs: From communications to sensing and intelligence," *IEEE Journal on Selected Areas in Communications*, vol. 39, no. 10, pp. 2912–2945, 2021.
- [5] T. Liang, T. Zhang, and Q. Zhang, "Toward seamless localization and communication: A Satellite-UAV NTN architecture," *IEEE Network*, vol. 38, no. 4, pp. 103–110, 2024.
- [6] T. Liang, W. Liu, J. Yang, and T. Zhang, "Age of information based scheduling for UAV aided emergency communication networks," in *ICC 2022 - IEEE International Conference on Communications*, 2022, pp. 5128–5133.
- [7] T. Liang, T. Zhang, Q. Wu, W. Liu, D. Li, Z. Xie, D. Li, and Q. Zhang, "Age of information based scheduling for UAV aided localization and communication," *IEEE Transactions on Wireless Communications*, vol. 23, no. 5, pp. 4610–4626, 2024.
- [8] P. Pothana, J. Joy, P. Snyder, and S. Vidhyadharan, "Uas air-risk assessment in and around airports," in *2023 Integrated Communication, Navigation and Surveillance Conference (ICNS)*, 2023, pp. 1–11.
- [9] J. Yang, Y. Wang, X. Hang, and D. Delahaye, "A review on airspace design and risk assessment for urban air mobility," *IEEE Access*, vol. 12, pp. 157 599–157 611, 2024.
- [10] W. Yuan, C. Liu, F. Liu, S. Li, and D. W. K. Ng, "Learning-based predictive beamforming for UAV communications with jittering," *IEEE Wireless Communications Letters*, vol. 9, no. 11, pp. 1970–1974, 2020.
- [11] H. Jin, W. Yuan, J. Wu, J. Wang, D. Niyato, X. Wang, G. K. Karagiannidis, Z. Lin, Y. Gong, D. I. Kim *et al.*, "Advancing the control of low-altitude wireless networks: Architecture, design principles, and future directions," *arXiv preprint arXiv:2508.07967*, 2025.
- [12] Y. Wang, K. Zu, L. Xiang, Q. Zhang, Z. Feng, J. Hu, and K. Yang, "Isac enabled cooperative detection for cellular-connected UAV network," *IEEE Transactions on Wireless Communications*, vol. 24, no. 2, pp. 1541–1554, 2025.
- [13] J. Wu, W. Yuan, Q. Cheng, and H. Jin, "Toward dual-functional LAWN: Control-aware system design for aerodynamics-aided UAV formations," *arXiv preprint arXiv:2507.19910*, 2025.
- [14] A. P. Cohen, S. A. Shaheen, and E. M. Farrar, "Urban air mobility: History, ecosystem, market potential, and challenges," *IEEE Transactions on Intelligent Transportation Systems*, vol. 22, no. 9, pp. 6074–6087, 2021.
- [15] C. Dong, Y. Wang, W. Wang, X. Zhu, M. Zhang, and Q. Wu, "Low-altitude centric space-air-ground integrated network: Evolutions, challenges and countermeasures," *IEEE Internet of Things Journal*, pp. 1–2025.
- [16] X. Huang, Z. Wang, Q. Peng, H. Xu, and Z. He, "LSS UAV target intelligent detection in urban complex environment," in *2021 IEEE 3rd International Conference on Civil Aviation Safety and Information Technology (ICCASIT)*, 2021, pp. 648–650.
- [17] G. Lei, T. Liang, Y. Ping, X. Chen, L. Zhou, J. Wu, X. Zhang, H. Ding, X. Zhang, W. Yuan *et al.*, "Enhancing low-altitude airspace security: Mllm-enabled UAV intent recognition," *arXiv preprint arXiv:2509.06312*, 2025.
- [18] Z. Li, Z. Gao, K. Wang, Y. Mei, C. Zhu, L. Chen, X. Wu, and D. Niyato, "Unauthorized UAV countermeasure for low-altitude economy: Joint communications and jamming based on MIMO cellular systems," *IEEE Internet of Things Journal*, vol. 12, no. 6, pp. 6659–6672, 2025.
- [19] M. Liu, H. Xiao, G. Pan, J. Zhou, W. Li, and X. Xi, "How to achieve large-scale development in the low-altitude economy," in *2024 IEEE 10th International Symposium on Microwave, Antenna, Propagation and EMC Technologies for Wireless Communications (MAPE)*, 2024, pp. 1–4.
- [20] T. Liang, T. Zhang, S. Zhou, W. Liu, D. Li, and Q. Zhang, "UAV-aided localization and communication: Joint frame structure, beamwidth, and power allocation," *IEEE Journal of Selected Areas in Sensors*, vol. 1, pp. 154–165, 2024.
- [21] T. Liang, H. Ding, Y. Ping, T. Zhang, L. Zhou, Q. Zhang, and T. Q. S. Quek, "Satellite-assisted uav control: Sensing and communication scheduling for energy efficient data collection," *IEEE Internet of Things Journal*, pp. 1–1, 2025.
- [22] R. Niu, Y. Qu, and Z. Wang, "UAV detection based on improved yolov4 object detection model," in *2021 2nd International Conference on Big Data & Artificial Intelligence & Software Engineering (ICBASE)*, 2021, pp. 25–29.
- [23] Z. Wang, Z. Cao, J. Xie, W. Zhang, and Z. He, "Rf-based drone detection enhancement via a generalized denoising and interference-removal framework," *IEEE Signal Processing Letters*, vol. 31, pp. 929–933, 2024.
- [24] M. Ezuma, F. Erden, C. Kumar Anjinappa, O. Ozdemir, and I. Guvenc, "Detection and classification of UAVs using rf fingerprints in the presence of wi-fi and bluetooth interference," *IEEE Open Journal of the Communications Society*, vol. 1, pp. 60–76, 2020.
- [25] W. Xie, Y. Wan, G. Wu, Y. Li, F. Zhou, and Q. Wu, "An RF-Visual directional fusion framework for precise UAV positioning," *IEEE Internet of Things Journal*, vol. 11, no. 22, pp. 36 736–36 747, 2024.

[26] W. Yuan, Z. Wei, S. Li, J. Yuan, and D. W. K. Ng, "Integrated sensing and communication-assisted orthogonal time frequency space transmission for vehicular networks," *IEEE Journal of Selected Topics in Signal Processing*, vol. 15, no. 6, pp. 1515–1528, 2021.

[27] M. Jia, J. Yang, and T. Zhang, "Power allocation in infrastructure limited integration sensing and localization wireless networks," in *2022 IEEE 96th Vehicular Technology Conference (VTC2022-Fall)*, 2022, pp. 1–5.

[28] F. Liu, W. Yuan, C. Masouros, and J. Yuan, "Radar-assisted predictive beamforming for vehicular links: Communication served by sensing," *IEEE Transactions on Wireless Communications*, vol. 19, no. 11, pp. 7704–7719, 2020.

[29] F. Liu, Y. Cui, C. Masouros, J. Xu, T. X. Han, Y. C. Eldar, and S. Buzzi, "Integrated sensing and communications: Toward dual-functional wireless networks for 6G and beyond," *IEEE journal on selected areas in communications*, vol. 40, no. 6, pp. 1728–1767, 2022.

[30] H. He, T. Liang, and T. Zhang, "Robust beamforming for isac systems in highly dynamic scenarios," in *2023 IEEE 34th Annual International Symposium on Personal, Indoor and Mobile Radio Communications (PIMRC)*, 2023, pp. 1–6.

[31] X. Zhang, W. Yuan, C. Liu, J. Wu, and D. W. K. Ng, "Predictive beamforming for vehicles with complex behaviors in ISAC systems: A deep learning approach," *IEEE Journal of Selected Topics in Signal Processing*, vol. 18, no. 5, pp. 828–841, 2024.

[32] Z. Yan, W. Yuan, X. Zhang, C. Liu, J. Wu, and T. Q. Quek, "Deep learning-based compensation mechanism for UAV sensing via OTFS signaling," *IEEE Internet of Things Journal*, 2025.

[33] J. Wu, W. Yuan, X. Zhang, Y. Yu, Y. Cui, F. Liu, G. Sun, J. Wang, D. Niyato, and D. I. Kim, "Toward multi-functional LAWNs with ISAC: Opportunities, challenges, and the road ahead," *arXiv preprint arXiv:2508.17354*, 2025.

[34] J. Wu, W. Yuan, and L. Hanzo, "When UAVs meet ISAC: Real-time trajectory design for secure communications," *IEEE Transactions on Vehicular Technology*, vol. 72, no. 12, pp. 16 766–16 771, 2023.

[35] Y. Zhao and Y. Su, "Estimation of micro-doppler parameters with combined null space pursuit methods for the identification of LSS UAVs," *IEEE Transactions on Geoscience and Remote Sensing*, vol. 61, pp. 1–11, 2023.

[36] P. Zhu, L. Wen, D. Du, X. Bian, H. Fan, Q. Hu, and H. Ling, "Detection and tracking meet drones challenge," *IEEE Transactions on Pattern Analysis and Machine Intelligence*, vol. 44, no. 11, pp. 7380–7399, 2022.

[37] Q. Wang, X. Wei, and M. Gao, "Lssdnet: A low-slow-small target detection method based on centimeter wave radar in the urban environment," *IEEE Sensors Journal*, vol. 25, no. 12, pp. 22 118–22 137, 2025.

[38] A. A. Selvi and S. P. K. Babu, "Design and simulation of an FMCW/CW X-Band radar for detection/classification of LSS targets," in *2025 International Conference on Wireless Communications Signal Processing and Networking (WiSPNET)*, 2025, pp. 1–6.

[39] W. Yuan, X. Chen, X. Du, J. Guan, J. Wang, and T. Lan, "A low slow small target classification network model based on k-band radar dynamic multifeature data fusion," *IEEE Sensors Journal*, vol. 25, no. 1, pp. 1656–1668, 2025.

[40] Y. Ahirrao, R. P. Yadav, and S. Kumar, "Real-time UAV detection through RF signal analysis and machine learning," in *2024 IEEE Microwaves, Antennas, and Propagation Conference (MAPCON)*, 2024, pp. 1–4.

[41] R. Akter, V.-S. Doan, A. Zainudin, and D.-S. Kim, "Sparsely connected low complexity CNN for unmanned vehicles detection-sensing RF signal," *IEEE Transactions on Vehicular Technology*, vol. 73, no. 10, pp. 14 236–14 251, 2024.

[42] B. Gao, M. Jia, T. Zhang, and Q. Zhang, "Reliable target positioning in complicated environments using multiple radar observations," in *2021 IEEE Global Communications Conference (GLOBECOM)*, 2021, pp. 1–6.

[43] R. Feng, E. De Greef, M. Rykunov, H. Sahli, S. Pollin, and A. Bourdoux, "Multipath ghost recognition for indoor MIMO radar," *IEEE Transactions on Geoscience and Remote Sensing*, pp. 1–10, 2021.

[44] X. Wang, M. Jia, X. Meng, and T. Zhang, "Multipath ghosts mitigation for radar-based positioning systems," in *2022 IEEE 96th Vehicular Technology Conference (VTC2022-Fall)*, 2022, pp. 1–6.

[45] F. Kraus, N. Scheiner, W. Ritter, and K. Dietmayer, "The radar ghost dataset: An evaluation of ghost objects in automotive radar data," in *2021 IEEE/RSJ International Conference on Intelligent Robots and Systems (IROS)*, 2021, pp. 8570–8577.

[46] D. Gholzani, A. Omri, S. Bouallegue, H. Chamkhia, and R. Bouallegue, "Stochastic geometry-based analysis of joint radar and communication-enabled cooperative detection systems," in *2021 17th International Conference on Wireless and Mobile Computing, Networking and Communications (WiMob)*, 2021, pp. 325–330.

[47] J. Yang, T. Zhang, X. Wu, T. Liang, and Q. Zhang, "Efficient scheduling in space-air-ground-integrated localization networks," *IEEE Internet of Things Journal*, vol. 9, no. 18, pp. 17 689–17 704, 2022.

[48] G. Ji, C. Song, and H. Huo, "Detection and identification of low-slow-small rotor unmanned aerial vehicle using micro-doppler information," *IEEE Access*, vol. 9, pp. 99 995–100 008, 2021.

[49] Y. Sun, S. Abeywickrama, L. Jayasinghe, C. Yuen, J. Chen, and M. Zhang, "Micro-doppler signature-based detection, classification, and localization of small uav with long short-term memory neural network," *IEEE Transactions on Geoscience and Remote Sensing*, vol. 59, no. 8, pp. 6285–6300, 2021.

[50] T. Zhang, A. F. Molisch, Y. Shen, Q. Zhang, H. Feng, and M. Z. Win, "Joint power and bandwidth allocation in wireless cooperative localization networks," *IEEE Transactions on Wireless Communications*, vol. 15, no. 10, pp. 6527–6540, 2016.

[51] I. Bekkerman and J. Tabrikian, "Target detection and localization using mimo radars and sonars," *IEEE Transactions on Signal Processing*, vol. 54, no. 10, pp. 3873–3883, 2006.

[52] W. Yuan, N. Wu, B. Etzlinger, H. Wang, and J. Kuang, "Cooperative joint localization and clock synchronization based on gaussian message passing in asynchronous wireless networks," *IEEE Transactions on Vehicular Technology*, vol. 65, no. 9, pp. 7258–7273, 2016.

[53] E. M. Mohamed and M. M. Fouad, "OTFS-Based Proactive Dynamic UAV Positioning for High-Speed Train Coverage," *IEEE Open Journal of the Communications Society*, vol. 5, pp. 5718–5734, 2024.

[54] F. Zafari, A. Gkelias, and K. K. Leung, "A survey of indoor localization systems and technologies," *IEEE Communications Surveys & Tutorials*, vol. 21, no. 3, pp. 2568–2599, 2019.

[55] M. Jia, J. Chen, Y.-C. Liang, and P.-Y. Kam, "Optimum noncoherent detection of constant-envelope signals using received signal magnitudes–energy detection and amplitude detection," *arXiv preprint arXiv:2502.17897*, 2025.

[56] T. Wang, H. Xiong, H. Ding, and L. Zheng, "Tdoa-based joint synchronization and localization algorithm for asynchronous wireless sensor networks," *IEEE Transactions on Communications*, vol. 68, no. 5, pp. 3107–3124, 2020.

[57] A. M. Haimovich, R. S. Blum, and L. J. Cimini, "Mimo radar with widely separated antennas," *IEEE Signal Processing Magazine*, vol. 25, no. 1, pp. 116–129, 2008.

[58] T. Liang, J. Yang, and T. Zhang, "Uav aided vehicle positioning with imperfect data association," in *2021 IEEE 93rd Vehicular Technology Conference (VTC2021-Spring)*, 2021, pp. 1–6.

[59] T. Liang and T. Zhang, "Simultaneous localization and tracking for uav-enhanced positioning network," in *2023 IEEE 98th Vehicular Technology Conference (VTC2023-Fall)*, 2023, pp. 1–5.

[60] J. Yang, T. Liang, and T. Zhang, "Deployment optimization in uav aided vehicle localization," in *2021 IEEE 93rd Vehicular Technology Conference (VTC2021-Spring)*, 2021, pp. 1–6.

[61] H. Zhu, Z. Zhu, and F. Su, "Clutter properties and suppression methods of hyper sonic airborne radar," in *2018 14th IEEE International Conference on Signal Processing (ICSP)*, 2018, pp. 859–862.

[62] M. Ash, M. Ritchie, and K. Chetty, "On the application of digital moving target indication techniques to short-range FMCW radar data," *IEEE Sensors Journal*, vol. 18, no. 10, pp. 4167–4175, 2018.

[63] M. Ezuma, O. Ozdemir, C. K. Anjinappa, W. A. Gulzar, and I. Guvenc, "Micro-uav detection with a low-grazing angle millimeter wave radar," in *2019 IEEE Radio and Wireless Symposium (RWS)*, 2019, pp. 1–4.

[64] A. Kammoun, R. Couillet, F. Pascal, and M.-S. Alouini, "Optimal design of the adaptive normalized matched filter detector using regularized tyler estimators," *IEEE Transactions on Aerospace and Electronic Systems*, vol. 54, no. 2, pp. 755–769, 2018.

[65] S. Rahman and D. A. Robertson, "Radar micro-doppler signatures of drones and birds at k-band and w-band," *Scientific reports*, vol. 8, no. 1, p. 17396, 2018.

[66] M. Jian, Z. Lu, and V. C. Chen, "Experimental study on radar micro-doppler signatures of unmanned aerial vehicles," in *2017 IEEE Radar Conference (RadarConf)*. IEEE, 2017, pp. 0854–0857.

[67] H. Fu, S. Abeywickrama, L. Zhang, and C. Yuen, "Low-complexity portable passive drone surveillance via sdr-based signal processing," *IEEE Communications Magazine*, vol. 56, no. 4, pp. 112–118, 2018.

[68] M. Jia, S. Li, J. L. Kernev, S. Yang, F. Fioranelli, and O. Romain, "Human activity classification with radar signal processing and machine learning," in *2020 International Conference on UK-China Emerging Technologies (UCET)*, 2020, pp. 1–5.

[69] D. Vovchuk, M. Khobzei, V. Tkach, O. Eliashiv, O. Tzidki, K. Grotov, A. Glam, and P. Ginzburg, "Micro-doppler-coded drone identification via resonant tagging," *IEEE Transactions on Antennas and Propagation*, vol. 73, no. 6, pp. 3917–3927, 2025.

[70] A. Brewster and A. Balleri, "Extraction and analysis of micro-doppler signatures by the empirical mode decomposition," in *2015 IEEE Radar Conference (RadarCon)*, May 2015, pp. 0947–0951.

[71] N. Yu, J. Wu, C. Zhou, Z. Shi, and J. Chen, "Open set learning for rf-based drone recognition via signal semantics," *IEEE Transactions on Information Forensics and Security*, vol. 19, pp. 9894–9909, 2024.

[72] M. U. Khan, M. Dil, M. Z. Alam, F. A. Orakazi, A. M. Almasoud, Z. Kaleem, and C. Yuen, "Safespace mfnet: Precise and efficient multifeature drone detection network," *IEEE Transactions on Vehicular Technology*, vol. 73, no. 3, pp. 3106–3118, 2024.

[73] F. Liu, X. Sun, H. Zhang, Y. Wang, X. Qu, and X. Yang, "Multipath ghost suppression based on frequency domain filtering for through-the-wall radar," in *2024 IEEE International Conference on Signal, Information and Data Processing (ICSIDP)*, 2024, pp. 1–6.

[74] Y. Zhou, X. Huang, D. Zhang, B. Li, J. Zeng, and F. Wu, "5g-based measurements and characterizations of low-altitude tethered balloon multipath channel," in *2021 IEEE 93rd Vehicular Technology Conference (VTC2021-Spring)*, 2021, pp. 1–5.

[75] J. Liu, L. Kong, X. Yang, and Q. H. Liu, "First-order multipath ghosts' characteristics and suppression in mimo through-wall imaging," *IEEE Geoscience and Remote Sensing Letters*, vol. 13, no. 9, pp. 1315–1319, 2016.

[76] I. Trofymov, V. Tiutiunnyk, A. Dudush, A. Shevchenko, and I. Medinets, "Deghosting method for multistatic radar systems with cooperative receiving," in *2020 IEEE Ukrainian Microwave Week (UkrMW)*, 2020, pp. 1–4.

[77] A. T. Abdalla and A. H. Muqaibel, "Single-view bistatic sparse reconstruction in twri exploiting ghost's aspect dependence feature," in *2016 IEEE Wireless Communications and Networking Conference*, 2016, pp. 1–5.

[78] H. Li, G. Cui, S. Guo, L. Kong, and X. Yang, "Target tracking and ghost mitigation based on multi-view through-the-wall radar imaging," in *2020 IEEE Radar Conference (RadarConf20)*, 2020, pp. 1–5.

[79] R. Feng, E. De Greef, M. Rykunov, H. Sahli, S. Pollin, and A. Bourdoux, "Multipath ghost recognition for indoor mimo radar," *IEEE Transactions on Geoscience and Remote Sensing*, pp. 1–10, 2021.

[80] F. Kraus, N. Scheiner, W. Ritter, and K. Dietmayer, "Using machine learning to detect ghost images in automotive radar," in *2020 IEEE 23rd International Conference on Intelligent Transportation Systems (ITSC)*, 2020, pp. 1–7.

[81] J. Shen and A. F. Molisch, "Estimating multiple target locations in multipath environments," *IEEE Transactions on Wireless Communications*, vol. 13, no. 8, pp. 4547–4559, 2014.

[82] M. Z. Win, Y. Shen, and W. Dai, "A theoretical foundation of network localization and navigation," *Proceedings of the IEEE*, vol. 106, no. 7, pp. 1136–1165, 2018.

[83] T. Liang, T. Zhang, B. Cao, and Q. Zhang, "Sensing, communication, and control co-design for energy-efficient UAV-aided data collection," *IEEE Wireless Communications Letters*, vol. 13, no. 10, pp. 2852–2856, 2024.

[84] T. Zhang, C. Qin, A. F. Molisch, and Q. Zhang, "Joint allocation of spectral and power resources for non-cooperative wireless localization networks," *IEEE Transactions on Communications*, vol. 64, no. 9, pp. 3733–3745, 2016.

[85] T. Liang, Z. Yu, T. Zhang, S. Zhou, W. Liu, D. Li, and Z. Niu, "Joint frame structure and beamwidth optimization for integrated localization and communication," in *2024 IEEE Wireless Communications and Networking Conference (WCNC)*, 2024, pp. 1–6.

[86] B. Peng, G. Seco-Granados, E. Steinmetz, M. Fr?hle, and H. Wymeersch, "Decentralized scheduling for cooperative localization with deep reinforcement learning," *IEEE Transactions on Vehicular Technology*, vol. 68, no. 5, pp. 4295–4305, 2019.

[87] C. Yang, F. Liu, and T. Zhang, "MSE based resource optimization in wireless localization networks," in *2021 IEEE 93rd Vehicular Technology Conference (VTC2021-Spring)*, 2021, pp. 1–6.

[88] M. A. Richards, *Fundamentals of radar signal processing*, 2nd ed, 2014.

[89] ———, *Fundamentals of radar signal processing*. Tata McGraw-Hill Education, 2005.

[90] L. Liu, J. Xu, G. Wang, X. Xia, Y. Gao, and T. Long, "An extended dimension music method for doa estimation of multiple real-valued sources," in *2016 CIE International Conference on Radar (RADAR)*, Oct 2016, pp. 1–5.

[91] V. C. Chen, F. Li, S.-S. Ho, and H. Wechsler, "Micro-doppler effect in radar: phenomenon, model, and simulation study," *IEEE Transactions on Aerospace and electronic systems*, vol. 42, no. 1, pp. 2–21, 2006.

[92] P. Sathe, A. Dyana, K. P. Ray, D. Shashikiran, and A. Vengadarajan, "Helicopter main and tail rotor blade parameter extraction using micro-doppler," in *2018 19th International Radar Symposium (IRS)*, June 2018, pp. 1–10.

[93] V. C. Chen and I. Ebrary, "The micro-doppler effect in radar," 2011.

[94] T. Liang, T. Zhang, J. Yang, D. Feng, and Q. Zhang, "UAV-aided positioning systems for ground devices: Fundamental limits and algorithms," *IEEE Internet of Things Journal*, vol. 9, no. 15, pp. 13470–13485, 2022.

[95] Y. Shen and M. Z. Win, "Fundamental limits of wideband localization part i: A general framework," *IEEE Transactions on Information Theory*, vol. 56, no. 10, pp. 4956–4980, 2010.